

The enhanced efficiency to 3.6% based on organic dye as donor and Si/TiO₂ acceptor bulk hetero-junction solar cells



Abdullah G. Al-Sehemi ^{a,b,c,*}, Ahmad Irfan ^{a,*}, Mohrah Abdullah M. Al-Melfi ^a, Ahmed A. Al-Ghamdi ^d, E. Shalaan ^d

^a Department of Chemistry, Faculty of Science, King Khalid University, PO Box 9004, Abha 61413, Saudi Arabia

^b Unit of Science and technology, Faculty of Science, King Khalid University, PO Box 9004, Abha 61413, Saudi Arabia

^c Center of Excellence for Advanced Materials Research, King Khalid University, PO Box 9004, Abha 61413, Saudi Arabia

^d Faculty of Science, Department of Physics, King Abdulaziz University, PO 80203, Jeddah 21589, Saudi Arabia

ARTICLE INFO

Article history:

Received 15 November 2013

Received in revised form 25 June 2014

Accepted 9 July 2014

Available online 17 July 2014

Keywords:

Organic-inorganic hybrid solar cells

Electronic properties

Fabrication

Efficiency

Density functional theory

Time dependent density functional theory

ABSTRACT

The efficient organic dyes 2-[4-[2-(2-hydroxybenzylidene)hydrazino]phenyl]ethylene-1,1,2-tricarbonitrile and 2-[4-[2-(4-hydroxybenzylidene)hydrazino]phenyl]ethylene-1,1,2-tricarbonitrile have been synthesized, characterized and fabricated as hetero-junction solar cell materials. We use B3LYP/6-31G*, B3LYP/6-31G** and HF/6-31G** level of theories to optimize the ground state geometries. The absorption wavelengths have been computed by using time dependent density functional theory which is in good agreement with the experimental data. The hetero-junction solar cell devices have been fabricated by organic-inorganic heterojunction (dye/Si/TiO₂) and measured the efficiency by applying the incident power 30, 50 and 70 mW/cm². The maximum efficiency 3.6% for dye2 has been observed. We shed light on the electronic and charge transport properties. Moreover, the stability and external quantum efficiencies have been measured.

© 2014 Elsevier B.V. All rights reserved.

1. Introduction

No doubt the efficiency of conventional solar cells made from inorganic materials reached up to 24% [1] and 25% [2] but this technology is very expensive. New ways to achieve low cost, easy to fabricate and environmental friendly solar cells alternatives to inorganic semiconductors are required. The organic solar cells achieved 10% efficiency [1] but inorganic materials are more stable than the organic counterparts [3]. The dye-sensitized solar cells (DSSCs) [4–7] and hybrid solar cells using the bulk heterojunction concept with different nanoparticles such as TiO_x [8], ZnO [9], CdSe [10,11], CdS [12], PbS [13], CuInS₂ [14,15] are attracting attention in recent years. The organic-inorganic (Si) hybrid solar cells have been also studied and proved an efficient technology [16a]. The efficiency has been obtained from 1.15 to 10.3% by varying the donor (organic material) and shape of the Si [16b–16g].

In organic-inorganic hybrid solar cells generally organic and inorganic parts have been combined with the aim to gain the advantages coupled with both material groups [17]. The solar cell devices having inorganic materials could support to overcome the photo-induced degradation of the conjugated organic materials. Moreover, the excitons which absorbed in the inorganic materials would lead to the photogeneration of charge carriers [18]. Still the efficiencies of hybrid solar cells are lower than that of polymer: fullerene devices but the issue of stability is major problem in this technology. On other hand, the most important issues in organic-nanoparticles hybrid solar cells are related to the nanoparticle surface chemistry and the nanomorphology of the photoactive layer.

Recently, we have synthesized and characterized the 2-[4-[2-4-methoxybenzylidenehydrazino]phenyl]ethylene-1,1,2-tricarbonitrile, 2-[4-[2-(3,4-dimethoxybenzylidene)hydrazino]phenyl]ethylene-1,1,2-tricarbonitrile, 2-[4-[2-(4-nitrobenzylidene)hydrazino]phenyl]ethylene-1,1,2-tricarbonitrile, 2-[4-[2-p-chlorobenzylidenehydrazino]phenyl]ethylene-1,1,2-tricarbonitrile and 2-[4-[2-p-bromobenzylidenehydrazino]phenyl]ethylene-1,1,2-tricarbonitrile hydrazones [19]. Previously, we also found that by substituting the donor groups ICT can be improved [7]. Thus in the present study the donor group –OH has been

* Corresponding author at: Corresponding authors at: King Khalid University, Chemistry, Abha 61413, Saudi Arabia. Tel.: +096672418632; fax: +0096672418426.

E-mail addresses: agmasq@gmail.com (A.G. Al-Sehemi), [\(A. Irfan\).](mailto:irfahmad@gmail.com)

substituted at ortho (2-{4-[2-(2-hydroxybenzylidene)hydrazino]phenyl}ethylene-1,1,2-tricarbonitrile (dye1) and para positions (2-{4-[2-(4-hydroxybenzylidene)hydrazino]phenyl}ethylene-1,1,2-tricarbonitrile (dye2). It is expected that –OH at para position would be more favorable to stabilize the dye. Moreover, probably as a result of the superior electron donating character of the –OH group at the para position would more direct the electrons toward the bridge. In the best of our knowledge, no these dyes were studied previously with respect to hetero-junction solar cell materials.

With the aim to design and synthesize efficient stable materials having high efficiency, we focused on organic hybrid solar cells (dye/Si/TiO₂) which would have no concerns like organic solar cells, organic-nanoparticle hybrid solar cells and conventional solar cells (inorganic). The organic hybrid solar cells would have the advantages, i.e., improved stability due to inorganic part compared to the organic solar cells. This technology would be low cost and environmental friendly as compared to the inorganic/conventional solar cells. In first step donor–bridge–acceptor organic materials with improved intra-molecular charge transfer (ICT) were designed, see Fig. 1. The ground state geometries have been optimized by using density functional theory (DFT) at B3LYP/6-31G*, B3LYP/6-31G** and HF/6-31G** level of theories. The absorption spectra have been computed by using time dependent density functional theory (TDDFT) at three different levels of theories mentioned above in gas phase and solvents (CHCl₃, CH₃CN and C₂H₅OH). The FTIR spectra were computed and compared with the experimental evidences. After that the ionization potentials, electron affinities, reorganization energies and chemical descriptors have been discussed. We shed light on the charge transfer behavior of the newly designed systems as well as structures-properties relationship. This study deals in depth study of the hetero-junction solar cell materials, their fabrication, solar cell device characterization, FTIR, stability, efficiency, charge transport behavior and DFT investigations.

We have divided the manuscript as follow: first section deals with the computational and experimental methodology which has been adopted in the present study. In next section, we have discussed the charge transfer properties and chemical descriptors. The main focus of this study is detailed investigations about the fabrication techniques, stability and efficiency measurements.

2. Methodology

2.1. General experimental methods

The hydrazone derivatives were prepared through direct condensation between the corresponding aromatic aldehydes and phenyl hydrazine. Equimolar quantities of phenylhydrazine and the aldehydes were boiled in ethanol for an hour. The precipitated hydrazones were filtered, washed and dried. The pure hydrazones were obtained after recrystallization from ethanol (detail can be found in supporting information).

Infra-red (FTIR) spectra of crystalline compounds were determined using a Thermo scientific smart omni-transmission. ¹H and ¹³C nuclear magnetic resonance (NMR) spectra were recorded on a Bruker at 500 MHz Ultra Shield™ at room temperature in deuterated dimethyl sulfoxide (DMSO-d₆) (CH₃SOCH₃ have two signals in ¹H-NMR at δ 2.52 singlet, 3.38 singlet). The UV-vis spectra were recorded with UV-1800 Shimadzu. Melting points (mps) were determined with a Stuart SMP11 without correction. Ultrasonic in which used an Elmasonic S 60H.

2.1.1. Physical data

For nuclear magnetic resonance (NMR) spectra, chemical shifts and expressed in ppm on the δ-scale relative to the internal

standard (TMS). The following abbreviations are used *s*—singlet, *t*—triplet, *q*—quartet, *d*—doublet, *m*—multiplet; *J* is the coupling constant (Hz).

2.1.2. General procedure for hydrazones

We have synthesized the hydrazone based sensitizers by the same method as in previous studies [19]. The hydrazone derivatives would be prepared through direct condensation between the corresponding aromatic aldehydes and phenyl hydrazine. Equimolar quantities of phenylhydrazine and the aldehydes would be boiled in ethanol for an hour. The precipitated hydrazones would be filtered, washed and dried. The pure hydrazones would be obtained after recrystallization from ethanol.

2.1.3. Preparation of 2-((2-phenylhydrazono)methyl)phenol (**1a**)

Salicylaldehyde (5.3 ml, 0.05 mol) was added to phenyl hydrazine (4.91 ml, 0.05 mol) and added 30 ml of ethanol absolute as solvent. The flask was related with condenser under reflux system and solution boiled at 170–180 °C for 1 h then transfer solution to beaker and stilled in room temperature or cooled, the precipitated hydrazones would be collected and filtered, washed with ethanol then dried. The product crystallization from ethanol gave yellow crystals of title compound (2-((2-phenylhydrazono)methyl)phenol) m.p 133–135 °C. δ H (DMSO, 500 MHz) 6.78–7.56 (9H, m, Ar-H), 8.2 (1H, s, CH=N), 10.42 (1H, s, OH), 10.55 (1H, s, NH); δ C (DMSO, 500 MHz) 111.70–144.72 (10C–Ar), 155.64 (CH=N).

2.1.4. Preparation of 4-((2-phenylhydrazono)methyl)phenol (**2a**)

The 4-hydroxybenzaldehyde (6.1 g, 0.05 mol) was added to phenylhydrazine (4.9 ml, 0.05 mole) and added 30 ml of ethanol absolute as solvent. The flask was related with condenser under reflux system and solution boiled at 170–180 °C for 1 h then transfer solution to beaker and stilled in room temperature or cooled, the precipitated hydrazones would be collected and filtered, washed with ethanol then dried. The product crystallization from ethanol gave yellow crystals of title compound (4-((2-phenylhydrazono)methyl)phenol m.p 164 °C. δ H (DMSO, 500 MHz) 6.69–7.49 (9H, m, Ar-H), 7.79 (1H, s, CH=N), 9.68 (1H, s, OH), 9.80 (1H, s, NH); δ C (DMSO, 500 MHz), 112.92, 115.63, 118.11, 126.88, 127.14, 128.65, 137.11 and 145.68(10C–Ar), 157.67 (CH=N).

2.1.5. General procedure for dyes

The new chromospheres were prepared by direct tricyanovinylation of hydrazones. A solution of the requisite hydrazone 1 (0.01 mol) and tetracyanoethylene (TCNE) in DMF (20 ml) was stirred at 60–90 °C for 8–12 h or boiled at high temperature up to 400 °C for 8 h. The solvent was removed and the residual solid was collected and recrystallized from toluene/petroleum ether mixture.

2.1.6. Preparation of 2-{4-[2-(2-hydroxybenzylidene)hydrazino]phenyl}ethylene-1,1,2-tricarbonitrile (dye1)

The 2-((2-phenylhydrazono)methyl)phenol (**1a**) (2.12 g, 0.01 mol) was dissolved in 20 ml DMF as solvent then added 1.28 g of TCNE direct gave dark color. The solution was boiled at 400 °C under reflux for 6 h. The solvent was removed and the residual solid collected and recrystallized from toluene/petroleum ether mixture to get dye1 (0.72 g, 23% yield) m.p 225–227 °C. δ H (DMSO, 500 MHz) 6.87–7.99 (8H, m, Ar-H), 8.45 (1H, s, CH=N), 10.2 (1H, s, OH exchange with D₂O), 11.84 (s, 1H, NH exchange with D₂O); δ C (DMSO, 500 MHz) 78.69 and 142.28 (C=C), 114.01, 114.24 and 114.79 (3xC≡N), 112.72, 115.87, 119.25, 120.16, 125.27, 128.86, 132.78, 136.90, 150.94 and 156.39 (10C–Ar), 162.27(CH=N).

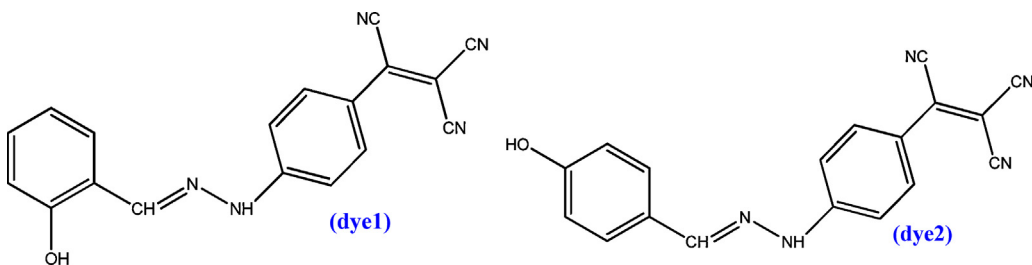


Fig. 1. The synthesized organic dyes in the present study.

2.1.7. Preparation of 2-{4-[2-(4-hydroxybenzylidene)hydrazino]phenyl}ethylene-1,1,2-tricarbonitrile (dye2)

The 4-((2-phenylhydrazono)methyl)phenol (**2a**) (2.12 g, 0.01 mol) was dissolved in 20 ml DMF as solvent then added 1.28 g of TCNE direct which gave dark color then the solution was boiled at 320–350 °C under reflux for 8 h. The solvent was removed and the solid residual was collected and recrystallized from toluene/petroleum ether mixture to get violet crystals of (dye2) m.p >300 °C. δ H (DMSO) 6.84–7.99 (8H, m, Ar-H), 8.06 (1H, s, CH=N), 10.01 (1H, s, OH exchange with D₂O), 11.75 (1H, s, NH exchange with D₂O); δ C (DMSO) 77.60 and 145.50 (C=C), 114.22, 114.41 and 114.87 (3xC≡N), 112.75, 115.77, 119.03, 125.15, 128.86, 132.80, 136.58 and 151.29 (8C-Ar), 159.50 (CH=N).

2.1.8. Solar cell device fabrication

The Si wafer was immersed for 10 s in HF solution (water/HF 49%) for etching purpose. Then it was rinsed in a mixture of ethanol, acetone and de-ionized water with molar ratios 1:1:3, respectively, to eliminate the fluoride ions. The substrates were rinsed with dry nitrogen gas. Recently we showed that the nanoporous TiO₂ prepared by sol-gel method from the mixture of H₂O₂ and HNO₃ has better porosity about 32% and showed only pure anatase phase with energy gap of 3.2 eV [20a]. The sol-gel method is a favorable method to prepare nanocrystalline/amorphous porous materials [20b]. The estimated porous size is about 30–40 nm (diameter). The SEM image shows deep porous sponge-like structure (see Supporting information and Ref. [20a]). The sol-gel solution was used to deposit a TiO₂ films on glass and silicon substrates by spin-coating method. All films were prepared at spin-coated at rate 2000 rpm (revolution per minute) for 1 min on pre-cleaned substrates (glass and SiO₂ etched-silicon), then dried in oven (60 °C for 10 min). For building solar cell device; about 20 nm nanoporous TiO₂ film has been deposited on SiO₂ etched-Si substrate having porosity 32% [20a]. Then about 400 nm of dye was deposited on the top of TiO₂ film. By inserting nanoporous TiO₂ between the dye (active layer) and metal electrode enable the active layer to harvest more light and increasing optical absorption in four ways: increasing the surface area and roughness, increasing the charge collection efficiency, helping as a blocking layer for holes, and reducing the recombination rate [21a]. Gold has been used as a top metal electrode by use of a suitable mask to control the shape of the electrode.

The dye thin films were prepared by conventional thermal evaporation technique at a pressure of about 10⁻⁶ mbar. The powder was loaded into a molybdenum cell with nozzle of 2 mm in diameter on the top. The flat glass; glass coated-TiO₂; and silicon substrates were located above 20 cm from the dye. The films were deposited at room temperature and the rate of deposition was 0.2 nm s⁻¹. The low deposition rate was adjusted for better film quality and crystallinity [21b]. The dye layer was prepared by thermal evaporation on the etched surface of Si substrate.

2.1.9. Solar cell device characterization

For solar cell device characterization a combination of software and hardware has been used. Before initiate of characterization process for our fabricated solar cell device, the light and circuit setup was tested by measuring the I-V curve of a reference 2 × 2 cm calibrated solar cell made of Si from Oriel. The solar reference cells come with a certificate of calibration accredited by NIST to the ISO-17025 standard and is traceable both to the National Renewable Energy Laboratory (NREL), and to the International System of Units (SI).

Au back contact of thickness about 100 nm was evaporated on a fabricated solar cell sample by use of thermal evaporation technique in working pressure of 10⁻⁶ mbar. A device area of (20 × 9) mm was identified by an evaporation mask. The masked solar cell device was tested under a solar simulator (Oriel Sol3A Class AAA Solar Simulators with illuminated area 8 × 8 in) at AM1.5 with 30, 50 and 70 mW/cm² illumination conditions adjusted and calibrated by use of a Skye SKS1110 sensor. Finally, the I-V curve was registered by use of Keithley Model 4200-SCS semiconductor characterization system using a scan rate of 1 mV/s.

2.2. Computational details

The DFT [22] is good approach to reproduce the experimental data and to predict the properties of interests. The B3LYP has been proved an efficient approach to reproduce the experimental data for the small molecules [23]. Moreover, by using the large fraction of HF exchange charge transfer states have been discussed previously [24]. The TD-B3LYP functional has been applied to compute and reproduce the absorption wavelengths of different organic dyes (indigo, azobenzene, phenylamine, hydrazone, and anthraquinone) and 0.12 eV average deviation was observed for hydrazone dyes [25]. Recently, it was pointed out that the B3LYP was good choice to reproduce the excitation energies for hydrazone based dyes. It was found that B3LYP (polarizable continuum model (PCM), methanol) is better, accurate and more reasonable choice than BH&HLYP, LC-BLYP and CAM-B3LYP (PCM, methanol) to reproduce the experimental data (Details can be found in Ref. [26]). In the present study we have computed the excitation energies by using B3LYP functional. The effect of solvents (CHCl₃, CH₃CN and C₂H₅OH) has been studied on the absorption spectra.

Geometry optimizations for all dyes have been performed using DFT at the B3LYP/6-31G*, B3LYP/6-31G** [27–30] and Hartree-Fock (HF) at HF/6-31G** [31] level of theories. The vibrational modes were examined by using the Chemcraft program [32]. The absorption spectra and energy gap for dyes were calculated in different solvents (PCM) at TD-B3LYP/6-31G* level of theory [33–35]. The ionization potentials, electron affinities and reorganization energy of all dyes have been performed by using the B3LYP/6-31G* level of theory [36,37]. The PCM [38–41] has been used for evaluating bulk solvent effects at all stages. All of the calculations were performed by using Gaussian-09 program package [42].

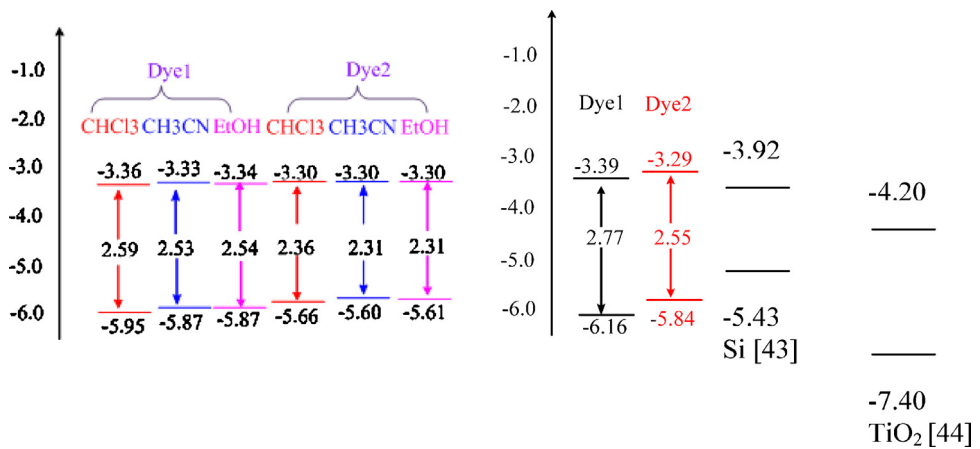


Fig. 2. The HOMOs energies, LUMOs energies and energy gaps of dyes in different solvents (left), gas phase (right) and acceptor materials (in eV).

3. Results and discussion

3.1. Electronic properties and absorption spectra

The computed highest occupied molecular orbitals (HOMOs) energies (E_{HOMO}), lowest unoccupied molecular orbitals (LUMOs) energies (E_{LUMO}) and HOMO–LUMO energy gaps (E_{gap}) have been illustrated in Fig. 2. In solvents, the E_{HOMO} level elevated as compared to gas phase. The E_{HOMO} of dye1 in CHCl₃, CH₃CN and C₂H₅OH are –0.21, –0.29 and –0.29 eV higher than that of the E_{HOMO} without solvent, respectively. The E_{HOMO} of dye2 in CHCl₃, CH₃CN and C₂H₅OH are –0.18, –0.24 and –0.23 eV are elevated compared to the E_{HOMO} without solvent, respectively. The solvents have no significant effect to elevate or diminish the E_{LUMO} . The root cause of reduced E_{gap} in solvents is the elevation of E_{HOMO} . The effect of CH₃CN and C₂H₅OH solvents on the E_{HOMO} and E_{LUMO} is similar to lift up or reduce resulting corresponding E_{gap} . The larger E_{gap} in CHCl₃ revealing that all the studied dyes would be red shifted in CH₃CN and C₂H₅OH solvents.

The E_{HOMO} and E_{LUMO} of Si are –5.43 and –3.92 eV [43] while the E_{HOMO} and E_{LUMO} of TiO₂ are –7.40 and –4.20 eV, respectively [44]. The Nested band alignment in the donor and acceptor frontier molecular orbitals was observed by considering the Si as acceptor. The successful operation of a photovoltaic device requires a staggered band alignment heterojunction which allocate electrons to transport to the cathode and holes to the anode. By considering the average values both for Si and TiO₂, the valance band energy has been found –6.41 eV while the conduction band energy –4.06 eV (Si/TiO₂). It is expected that Si/TiO₂ acceptor changed the alignment to staggered band alignment heterojunction, see Fig. 2, Tables S1 and S2.

In hybrid solar cells, excitons formed in the donor material are dissociated at the donor–acceptor (D–A) interface. The force required to overcome the exciton binding energy is provided by the energy level offset of the LUMO of the donor and the conduction band edge of the acceptor material. We found energy level offset 0.67 and 0.77 eV for dye1 and dye2, respectively, to overcome the exciton binding energy. It is revealing that in dye1 less force is required to overcome the exciton binding energy as compared to dye2. For dissociation of excitons formed in the acceptor material, the energy offset of the HOMO of the donor and the valence band edge of the acceptor material is required. The energy level offset 0.25 and 0.57 eV for dye1 and dye2, respectively, was noticed to dissociate of excitons. In dye1 less force would be required for dissociation of excitons as compared to dye2. It is expected that dye1 would be more efficient because of less force would be required

to overcome the exciton binding energy as well as dissociation of excitons.

The dye2 displayed a clearly red-shifted absorption wavelengths compared to dye1, probably as a result of the superior electron donating character of the –OH group at the para position which more directed the electrons toward the bridge and the tricyano moiety is more electron withdrawing in comparison with an dye1 when the –OH group is at the ortho position. Interestingly, for both dyes the absorption maxima in the most polar solvent (C₂H₅OH) were slightly red-shifted in comparison with those observed in the least polar one (CHCl₃). This behavior indicates possible partial protonation of the donor group due to the interaction with the polar protic medium.

By substituting the hydroxyl group at ortho position (dye1) showed absorption band at 514 nm in chloroform and 521 nm in CH₃CN. No significant effect has been observed in absorption spectra toward red shift by changing chloroform to CH₃CN. While substituting hydroxyl group at para position (dye2) showed absorption band at 531 nm in chloroform. The dyes were measured in various solvents having different polarity, see Table 1. The trend of absorption spectra toward red shift of dye1 and dye2 in different solvents is CHCl₃ < CH₃CN < CH₃CH₂OH. The maximum absorption spectra computed at TD-B3LYP/6-31G* level of theory in chloroform are 524 and 568 for dye1 and dye2, respectively. The maximum absorption wavelengths in acetonitrile are 529 and 574 eV for dye1 and dye2, respectively. In ethanol, the maximum absorption wavelengths at 529 and 574 nm for dye1 and dye2, respectively, have been discerned which are in reasonable agreement with the experimental evidences.

3.2. FTIR spectra

Vibrational spectral assignments have been performed on the recorded FTIR spectrum based on the theoretical predicted wavenumbers by DFT/B3LYP/6-31G*, B3LYP/6-31G** and HF/6-31G** level of theories. The computed wavenumbers by DFT are in good agreement with the experimental values. The FTIR spectra have been calculated for free molecules in vacuum while experiments have been performed for solid samples. For this reason scale factors in theoretical calculations were applied, i.e., 0.937 for DFT calculations and 0.860 and 0.850 for dye1 and dye2, respectively, for HF calculations.

The FTIR spectra exhibited three important absorption bands; the first band has been observed at 3261 and 3221 cm^{–1} for the ($\nu_{\text{N–H}}$) mode for dye1 and dye2, respectively. In the present case, DFT calculations gave band at 3361 and 3380 cm^{–1} at B3LYP/6-31G*

Table 1

Calculated (calc) and experimental (exp) absorption spectra and oscillator strength (f) in different solvents.

Calc	CHCl ₃				CH ₃ CN				EtOH			
	Exp		Calc		Exp		Calc		Exp		Calc	
	λ	(f)	λ	(f)	λ	(f)	λ	(f)	λ	(f)	λ	(f)
Dye1	514	0.1	524	0.57	521	0.17	529	0.56	539	0.31	529	0.56
	338	0.02	448	0.21	339	0.02	362	0.09	350	0.15	452	0.21
	289	0.004	360	0.1	287	0.004			298	0.04	362	0.09
Dye2	531	1.35	568	0.74	545	0.39	574	0.72	553	0.57	574	0.72
	335	0.24	409	0.22	333	0.21	415	0.23	333	0.06	415	0.23
	282	0.08	341	0.006	252	0.02	347	0.002	290	0.01	347	0.002

and 3379 and 3396 cm⁻¹ at B3LYP/6-31G**. The HF calculations gave band at 3462 and 3258 cm⁻¹ for dye1 and dye2, respectively. The NH stretching wavenumber is red shifted in FTIR from the computed wavenumber which indicates the weakening of the N–H bond resulting in hydrogen bonding. The strong and sharp second band appears in the region of 2219–2215 cm⁻¹ which was attributed to the cyano group. The B3LYP/6-31G* and B3LYP/6-31G** calculations gave these modes at 2201 and 2200 cm⁻¹ while HF gave at 2224 and 2223 cm⁻¹ for dye1 and dye2, respectively. The third absorption band in the region of 1600 and 1610 cm⁻¹ ascribed for the C=N in dye1 and dye2, respectively. The DFT calculations gave band at 1570 and 1581 cm⁻¹ at B3LYP/6-31G* level of theory and 1566 and 1577 cm⁻¹ at B3LYP/6-31G** level of theory. The HF calculations gave this mode at 1549 and 1627 cm⁻¹ for dye1 and dye2, respectively. The absorption of OH group appear in dye1 and dye2 in the range 3143–3443 cm⁻¹ (experimental FTIR measurements), from 3139 to 3577 cm⁻¹ for DFT and from 3261 to 3564 cm⁻¹ for HF method. The N–H stretching vibration showed only one band at 3335 cm⁻¹ [45]. The sharp band has been observed at 3265 cm⁻¹ in the FTIR spectrum. The DFT calculations showed band at 3361 and 3379 cm⁻¹ for B3LYP/6-31G* and B3LYP/6-31G**, respectively. The HF calculations gave band at 3462 cm⁻¹. Effect of hydrogen bonding on an O–H stretching vibration has been appeared in the region 3500–2500 cm⁻¹ [45]. The ν_{O-H} mode is interference with N–H stretching mode and observed broad band in the region about 3143 cm⁻¹. The DFT calculations gave band at 3139 and 3152 cm⁻¹ for B3LYP/6-31G* and B3LYP/6-31G** level of theories, respectively, while the HF gave at 3261 cm⁻¹.

For the existence of benzene rings in a structure, the C–H and C=C–C vibrations are varying and depending on the number and type of substitutions. The C=C stretching vibration showed in the region (1577 ± 4) cm⁻¹ and (1579 ± 6) cm⁻¹ [46]. In the present case the $\nu_{C=C}$ mode of aromatic rings occurred at 1656 cm⁻¹. The $\nu_{C=C}$ mode appeared at 1576 and 1573 cm⁻¹ at B3LYP/6-31G* and B3LYP/6-31G** level of theories, respectively. The C≡N stretching vibration has been reported in the range 2235–2215 cm⁻¹ [46]. The sharp and strong band for $\nu_{C\equiv N}$ mode appeared at 2219 cm⁻¹ in FTIR spectra. The DFT calculations gave $\nu_{C\equiv N}$ mode in the range 2178–2201 cm⁻¹ at B3LYP/6-31G* and B3LYP/6-31G** level of theories while HF showed band in the range 2217–2224 cm⁻¹.

The $\nu_{C\equiv N}$ mode has been reported in the range 1605–1665 cm⁻¹ by Asiri et al. [47]. In present case the strong band has been observed at 1601 cm⁻¹ in the FTIR spectra (C≡N stretching mode). The DFT calculations gave same mode at 1570 and 1566 cm⁻¹ at B3LYP/6-31G* and B3LYP/6-31G** level of theories, respectively. In HF calculations this mode has been observed at 1549 cm⁻¹. The C–O stretching mode in literature has been observed in the range 1000–1300 cm⁻¹ [45]. The ν_{C-O} mode was observed at 1294 cm⁻¹ in FTIR while calculations showed this band at 1250 and 1206 cm⁻¹ for DFT and HF, respectively. The C=C in aromatic rings showed band at 1598, 1588, 1494, 1456 cm⁻¹ [48]. The computed modes at different level of theories have been tabulated in Tables S3 and S4 (Detail can be found in supporting information and Fig. 3).

Table 2

The vertical and adiabatic ionization potentials (IP_{v/a}), vertical and adiabatic electronic affinities (EA_{v/a}), hole and electron reorganization energies ($\lambda(h/e)$) of hydrazone dyes (in eV) at the B3LYP/6-31G* level of theory.

Dyes	IP _v	IP _a	EA _v	EA _a	$\lambda(h)$	$\lambda(e)$
Dye1	7.26	7.49	2.26	1.89	0.387	0.674
Dye2	6.98	7.15	2.10	1.82	0.359	0.555

Table 3

The chemical descriptors of dye1 and dye2 computed at different levels of theories (in eV).

Dyes	χ	η	ω	S	μ	ω_i
B3LYP/6-31G*						
Dye1	4.78	1.39	8.22	0.69	9.21	30.51
Dye2	4.56	1.27	8.17	0.64	11.75	54.13
B3LYP/6-31G*						
Dye1	4.78	1.38	8.27	0.69	6.78	16.61
Dye2	4.56	1.27	8.17	0.64	10.53	43.50
HF/6-31G**						
Dye1	3.99	4.14	1.92	2.07	8.53	8.78
Dye2	3.80	4.04	1.79	2.02	10.69	14.14

3.3. Chemical descriptors

The vertical ionization potentials (IP_v), adiabatic ionization potentials (IP_a), vertical electron affinities (EA_v), adiabatic electron affinities (EA_a), hole reorganization energies $\lambda(h)$ and electron reorganization energies $\lambda(e)$ have been tabulated in Table 2. Previously, it was concluded that higher EA_v would be favorable for the generation of free hole [49]. The better hole transfer materials have smaller value of ionization potentials [50] while better electron transfer materials have higher electron affinities. The high EA_v of dye1 is revealing that it would be more appropriate to generate free electrons and holes. The calculated hole reorganization energies of dye1 and dye2 are smaller than the electron reorganization energies revealing that these dyes might be better hole transfer materials as well.

The electronegativity (χ), hardness (η), electrophilicity (ω), softness (S) and electrophilicity index (ω_i) at the B3LYP/6-31G*, B3LYP/6-31G**, and HF/6-31G** level of theories have been presented in Table 3. It has been observed that the trend of the electronegativity (χ), hardness (η), electrophilicity (ω), softness (S) and electrophilicity index (ω_i) at all the level of theories is similar. The χ and ω are larger for dye1. The η and S for dye1 have the highest values. The significant effect to reduce the ω_i has been observed in dye1.

3.4. Efficiency

The external quantum efficiency (EQE) can be measured by using the following equation.

$$EQE = \eta_{abs} \times \eta_{diff} \times \eta_{diss} \times \eta_{tr} \times \eta_{cc} \quad (1)$$

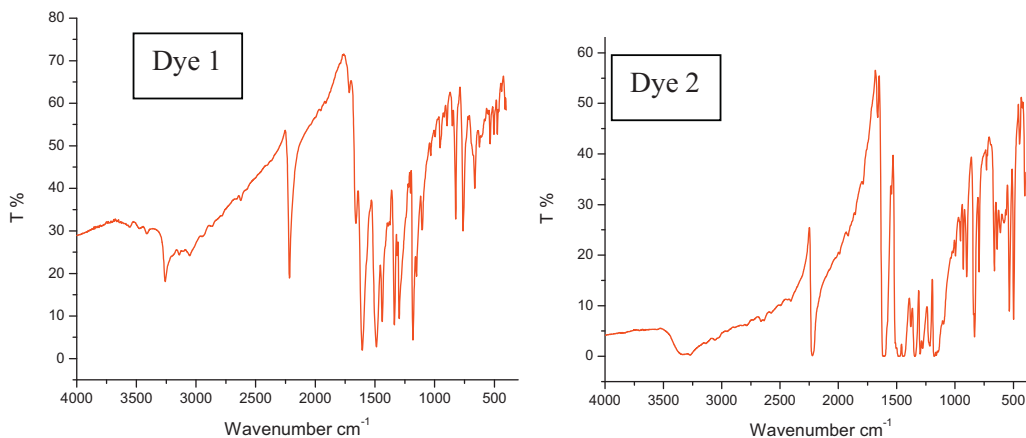


Fig. 3. The FTIR spectra of dye1 and dye2.

The short circuit current density (J_{sc}) is directly linked with the absorption yield (η_{abs}). In present case, not only the inorganic part is improving the absorption yield but the organic materials are also covering most of the absorption spectra revealing it can absorb more solar spectrum region. The next important parameter is η_{diff} describes the ability of an exciton to diffuse to a donor-acceptor (D-A) interface. This factor is inversely related to the rate of recombination within the photoactive material. The coplanarity between the benzene near anchoring group having LUMO and the bridge (N-N) is broken in studied dyes, i.e., 43° – 53° out-of-plane distortion, thus the, consequently hampering the recombination reaction. Ultimately this might enhance the ability of excitons to diffuse efficiently at the interface. The third parameter is the exciton dissociation yield (η_{diss}). As the electron is still bound within the exciton, the energy offset formed at the D-A interfaces is required to provide a driving force which releases the electron and allows conduction to occur. This energy offset must be larger than the excitonic binding energy in the material to facilitate charge transfer. This energy is typically in the range of 0.1–0.5 eV [51,52]. In present case 0.25 eV energy is required for dye1 which is in the above mentioned range.

The fourth parameter describes the efficiency of charge carrier transport throughout the device (η_{tr}). In organic materials, charge transport occurs via a process of hopping between energy states and is affected by traps and recombination sites in the photoactive film. The success of this transport depends greatly on the mobility of the associated semiconductors [53]. The recombination would be hampered and ultimately this would also enhance hopping/charge transport. Moreover, the dye1 has the high electron affinity which would improve the electron transport toward cathode.

The last important parameter describes the efficiency of charge collection at the electrodes (η_{cc}). The success of this step is greatly dependent on the electronic composition of the device. For successful injection of electrons into the cathode the magnitude of the conduction band edge energy level of the acceptor material with respect to the vacuum level must be lower than the work function of the metal. For successful injection of holes into the anode, the magnitude of the HOMO level of donor material must be higher than the work function of the transparent anode. The higher J_{sc} of dye2 is might be due to the above mentioned reasons. The higher FF value of dye2 is due to the less recombination occurring at the D-A interface.

Brabec et al. proposed an effective band gap model for bulk heterojunction cells; they correlated the maximum value of V_{oc} and the energy difference between the HOMO level of the donor and the LUMO level of the acceptor [54]. A linear relationship between electron affinity and V_{oc} was observed. In the present study, we have correlated the electron affinity of the donor material and V_{oc} .

Table 4
The organic-inorganic hybrid solar cell device performance parameters.

Complexes	Incident power (mW/cm ²)	V_{oc} (V)	J_{sc} (mA/cm ²)	FF	Efficiency (%)
Dye1	30	0.55	2.72	0.46	2.33
	50	0.58	4.72	0.49	2.72
	70	0.60	5.83	0.56	2.76
Dye2	30	0.45	2.73	0.51	2.10
	50	0.49	5.67	0.58	3.22
	70	0.53	7.80	0.61	3.58

It has been found that when the electron affinity increases generally the V_{oc} increases.

The relationship between diagonal band gap of the heterojunction and V_{oc} has been studied and no linear relationship was observed [55]. In the present study, the diagonal band gap of dye2 and dye1 have been observed, i.e., 2.10 and 1.78 eV, respectively. The V_{oc} have been observed 0.53 and 0.60 V, J_{sc} 7.80 and 5.83 mA/cm² while the FF 61.0 and 56.0% with 70 mW/cm² incident power. We didn't observe the linear relationship between the diagonal band gap and V_{oc} which is good agreement with previous study [55]. The larger diagonal band gap has been observed for dye2 resulting higher J_{sc} and FF.

Previously, a simple relationship between the HOMO of the donor material and the V_{oc} of the device was derived. Similarly, here linear relationship between the HOMO energies/ionization potential and the V_{oc} has been found. It was pointed out that if the LUMO energy level of donor material would be less than –3.92 eV, it can improve the efficiency of organic solar cell devices [56]. In present case, the LUMO of dye1 is smallest revealing that this would be the efficient donor.

The poly (3-hexylthiophene) is being used as efficient donor material in solar cell devices due to the enhanced absorption, environmental stability and higher hole mobility [57]. We have observed that the hole reorganization energy of dye2 is smaller than other counterpart revealing that it would be good donor material. Fig. 4 showed the current–voltage characteristics curves with open-circuit voltage and short-circuit current under different illumination power, i.e., 30, 50 and 70 mW/cm². The photovoltaic properties of heterojunction organic-inorganic hybrid solar cells (dye/Si/TiO₂) based on dye1 and dye2 have been shown in Table 4. The dye1 cell gave a short-circuit photocurrent density (J_{sc}) of 2.72 mA/cm², an open-circuit voltage (V_{oc}) 550 mV, and a fill factor (FF) of 46% with the illumination power (P_{in}) 30 mW/cm², corresponding to an overall conversion efficiency of 2.33%. The same device showed 2.72% efficiency with J_{sc} 4.72 mA/cm², V_{oc} 580 mV and FF of 49% when P_{in} is 50 mW/cm². By applying P_{in} 70 mW/cm²,

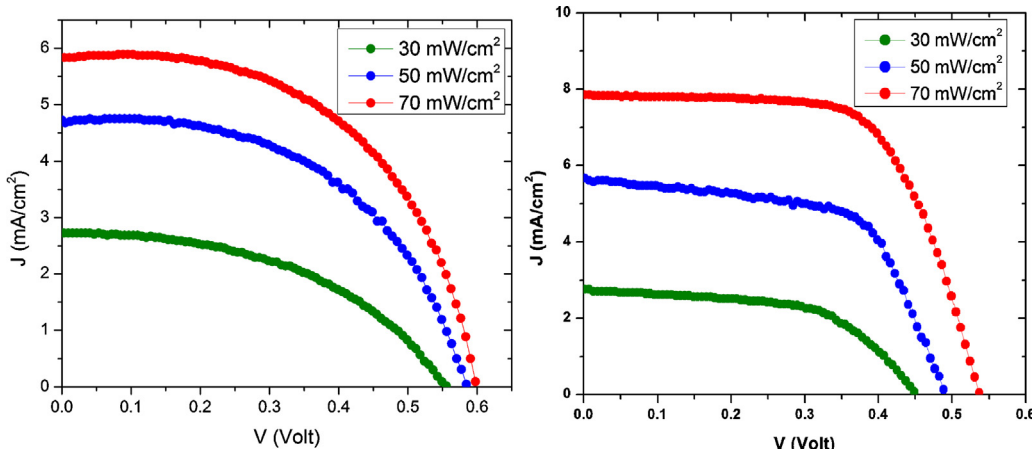


Fig. 4. The current-voltage characteristics curves with open-circuit voltage and short-circuit current under different illumination power left (dye1) and right (dye2).

the J_{sc} , V_{oc} and FF further improved to 5.83 mA/cm^2 , 600 mV and 56% , respectively, resulting efficiency enhanced to 2.76% . The dye2 gave J_{sc} 2.73 mA/cm^2 , V_{oc} of 450 mV and FF of 51% with P_{in} 30 mW/cm^2 leading power conversion efficiency 2.10% . The same system correspond J_{sc} 5.67 mA/cm^2 , V_{oc} of 490 mV and FF of 58% with P_{in} 50 mW/cm^2 consequential efficiency 3.22% . We observed 3.58% efficiency when the P_{in} was 70 mW/cm^2 which improved the J_{sc} , V_{oc} and FF to 7.80 mA/cm^2 , 530 mV and 61% , respectively. It can be noticed that by increasing the P_{in} from 30 mW/cm^2 to 70 mW/cm^2 J_{sc} , V_{oc} and FF improved resulting enhanced the efficiency, see Table 4.

3.5. Stability

Preliminary measurement results of the stability of dye1 and dye2 solar cells were reported. Here two basic accelerated tests

were used which are (i) constant temperatures exposure and (ii) temperature illumination stresses. In the first test, accelerated thermal stability was performed by store the dye1 and dye2 cells in the oven at 80°C for 240 h exposure period. Fig. 5 shows the temperature dependent of the characteristic parameters of the fabricated dye1 and dye2 cells. The change with temperature of V_{oc} and photovoltaic efficiency of dye2 was found to be less than that found in dye1. The efficiency of dye1 solar cell during 10 days of aging at 80°C showing a $\sim 15\%$ decrease while dye2 solar cell shows only 3% indicated very good stability.

In the temperature illumination stresses test which used to examine the photo-stability of the cells. Solar cells were exposed to continuous light soaking in a solar simulator tell the temperature of the cell reach 60°C . Fig. 6 illustrates the time evolution of the photovoltaic parameters where both cells show very good stabilities. The overall performance of the dye2 cell shows a very

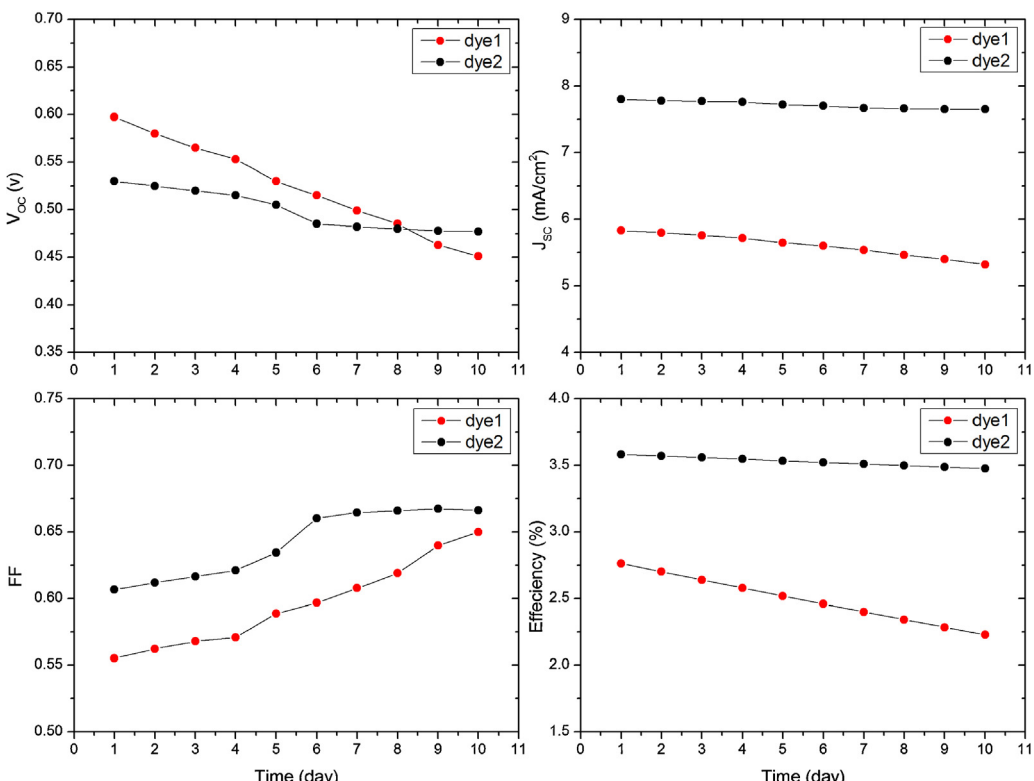


Fig. 5. Temporal evolution of dye1 and dye2 solar cells characteristic parameters under sequential thermal aging at 80°C .

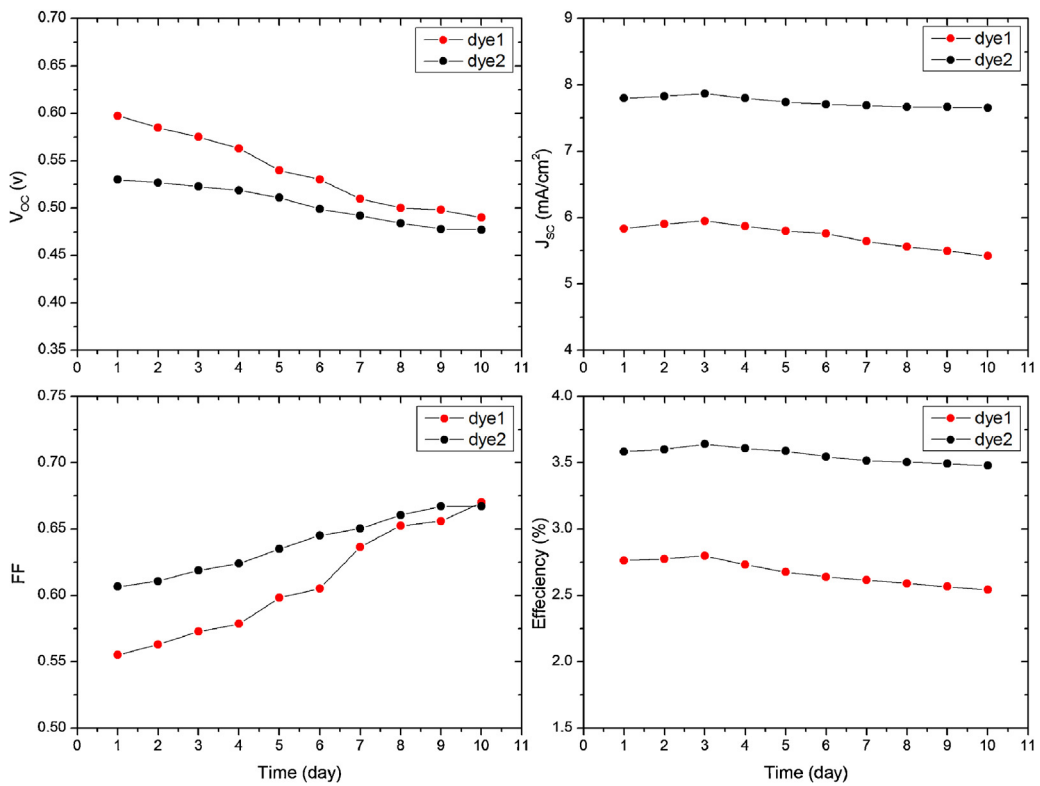


Fig. 6. Temporal evolution of dye1 and dye2 solar cells characteristic parameters under continuous light soaking at 60 °C.

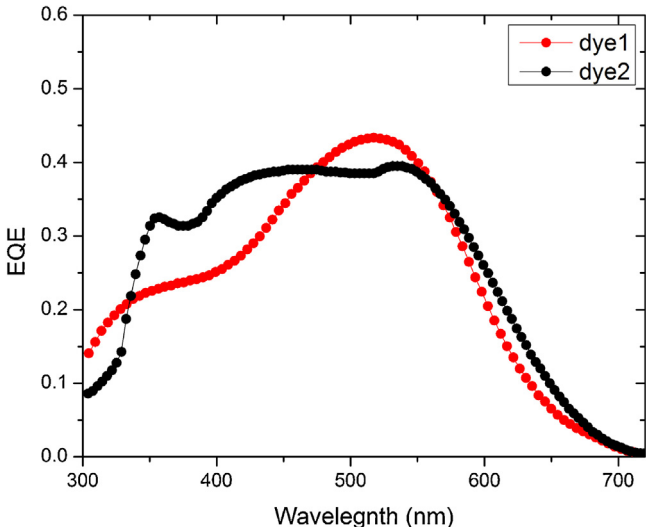


Fig. 7. External quantum efficiency (EQE) for the fabricated dye1 and dye2 solar cell devices (as indicated).

good stability while dye1 solar cell had decreased notably after 10 days of aging, due to the loss in V_{oc} and a lack of attenuation by J_{sc} .

3.6. External quantum efficiency

External quantum efficiency (EQE) spectra of the dye1 and dye2 cells are shown in Fig. 7. The maximum EQE value at 525 nm of the dye1 was approximately 45%, while the maximum EQE value for cell made from dye2 is 38% located at 550 nm. Generally, adsorbed spectrum of the dye2 cell is relatively higher than that of dye1 cell. In the region 330–480 nm the dye2 solar cell absorbed more spectra

than dye1 cell. The EQE spectrum of dye2 cell had a broad plateau region compared to the spectra of dye1 cell. Therefore, the cell made from dye2 can efficiently convert incident light to current in the region 350–650 nm.

Finally, the maximum EQE value for dye1 was observed at 525 nm while for dye2 at 550 nm. On other hand, the maximum absorption wavelength for dye1 and dye2 were found 514–529 and 531–574 nm by varying the solvents, respectively. These results showed that EQE and absorption spectra are almost similar. We observed some differences between the EQE and absorption spectra in the range of 350–450 nm, it is might be due to that the EQE were measured for cell while the absorption spectra in solvent.

4. Conclusions

The root cause of reduced energy gap in solvents is due to the elevation of HOMO energy level. The dye2 showed evidently red-shifted absorption wavelengths compared to dye1, probably due to the superior electron donating character of the –OH group at the para position. The absorption maxima in the most polar solvent were slightly red-shifted in comparison with those observed in the least polar one. The Si/TiO₂ acceptor might change the alignment to staggered band alignment heterojunction which would enhance the photovoltaic efficiency. The distortion in organic dye would hamper the recombination reaction which might enhance the ability of excitons to diffuse efficiently at the interface as well as improve charge carrier transport throughout the device. The smaller hole reorganization energy of dye2 revealed that it would be good donor material. The dye2 cell shows a fabulous stability while dye1 solar cell had decreased notably after 10 days of aging. It is expected that the cell made from dye2 can efficiently convert incident light to current in the region 350–650 nm. The bulk-heterojunction solar cell fabricated with dye2 film exhibited conversion efficiency of 3.6%. Moreover, the computed DFT

absorption and FTIR spectra were found in good agreement with the experimental evidences.

Acknowledgement

We thank King Abdul Aziz city of Science and Technology (KACST) for their financial support to Mohrah Abdullah M. Al-Melfi by the grant No. GSP-12-24.

Appendix A. Supplementary data

Supplementary data associated with this article can be found, in the online version, at <http://dx.doi.org/10.1016/j.jphotochem.2014.07.003>.

References

- [1] M.A. Green, K. Emery, Y. Hishikawa, W. Warta, E.D. Dunlop, Solar cell efficiency tables (version 39), *Prog. Photovoltaics Res. Appl.* 20 (2012) 12–20.
- [2] M. Green, *Prog. Photovoltaics Res. Appl.* 9 (2001) 123–135.
- [3] S. Ren, L.-Y. Chang, S.-K. Lim, J. Zhao, M. Smith, N. Zhao, V. Bulovic, M. Bawendi, S. Gradečák, *Nano Lett.* 11 (2011) 3998–4002.
- [4] G. Smestad, S. Spiekermann, J. Kowalik, C.D. Grant, A.M. Schwartzberg, J. Zhang, L.M. Tolbert, E. Moons, *Sol. Energy Mater. Sol. Cells* 76 (2003) 85–105.
- [5] D. Gebeyehu, C. Brabec, N.S. Sariciftci, D. Vangeneugden, R. Kiebooms, D. Vandervende, F. Kienberger, H. Schindler, *Synth. Met.* 125 (2001) 279–287.
- [6] L. Sicot, C. Fiorini, A. Lorin, J.M. Nunzi, P. Raimond, C. Sentein, *Synth. Met.* 102 (1999) 991–992.
- [7] A. Irfan, *Mater. Chem. Phys.* (2013), <http://dx.doi.org/10.1016/j.matchemphys.2013.07.011>.
- [8] P.A.V. Hal, M.M. Wienk, J.M. Kroon, W.J.H. Verhees, L.H. Sloff, W.J.H.V. Gennip, P. Jonkheijm, R.A.J. Janssen, *Adv. Mater.* 15 (2003) 118–121.
- [9] W.J.E. Beek, M.M. Wienk, R.A.J. Janssen, *Adv. Funct. Mater.* 16 (2006) 1112–1116.
- [10] A.P. Alivisatos, *Science* 271 (1996) 933–937.
- [11] W. Huynh, J. Dittmer, A.P. Alivisatos, *Science* 295 (2002) 2425–2427.
- [12] N.C. Greenham, X. Peng, A.P. Alivisatos, *Phys. Rev. B: Condens. Matter* 54 (1996) 17628–17637.
- [13] S. McDonald, G. Konstantatos, S. Zhang, P.W. Cyr, E.J.D. Klem, L. Levina, H. Sargent, *Nat. Mater.* 4 (2005) 138–142.
- [14] E. Arici, N.S. Sariciftci, D. Meissner, *Adv. Funct. Mater.* 13 (2003) 165–171.
- [15] E. Arici, D. Meissner, N.S. Sariciftci, in: H.S. Nalwa (Ed.), *Encyclopedia of Nanoscience and Nanotechnology*, 1, 2004, ISBN: 1-58883-001-2, Edited by Hari Singh Nalwa, USA.
- [16] (a) M. Wright, A. Uddin, *Sol. Energy Mater. Sol. Cells* 107 (2012) 87–111;
 (b) J.-S. Huang, C.-Y. Hsiao, S.-J. Syu, J.-J. Chao, C.-F. Lin, *Sol. Energy Mater. Sol. Cells* 93 (2009) 621–624;
 (c) H.-J. Syu, S.-C. Shiu, C.-F. Lin, *Sol. Energy Mater. Sol. Cells* 98 (2012) 267–272;
 (d) S.-C. Shiu, J.-J. Chao, S.-C. Hung, C.-L. Yeh, C.-F. Lin, *Chem. Mater.* 22 (2010) 3108–3113;
 (e) S.-H. Tsai, H.-C. Chang, H.-H. Wang, S.-Y. Chen, C.-A. Lin, S.-A. Chen, Y.-L. Chueh, J.-H. He, *ACS Nano* 5 (2011) 9501–9510;
 (f) L. He, *Appl. Phys. Lett.* 99 (2011) 021104;
 (g) C.-Y. Liu, Z.C. Holman, U.R. Kortshagen, *Adv. Funct. Mater.* 20 (2010) 2157–2164.
- [17] (a) Y. Zhou, M. Eck, M. Kruger, *Energy Environ. Sci.* 3 (2010) 1851–1864;
 (b) T. Xu, Q. Qiao, *Energy Environ. Sci.* 4 (2011) 2700–2720.
- [18] (a) Y. Zhou, M. Eck, C. Veit, B. Zimmermann, F. Rauscher, P. Niyamakom, S. Yilmaz, I. Dumsch, S. Allard, U. Scherf, M. Kruger, *Sol. Energy Mater. Sol. Cells* 95 (2011) 1232–1237;
 (b) D. Celik, M. Krueger, C. Veit, H.F. Schleiermacher, B. Zimmermann, S. Allard, I. Dumsch, U. Scherf, F. Rauscher, P. Niyamakom, *Sol. Energy Mater. Sol. Cells* 98 (2012) 433–440.
- [19] (a) A.G. Al-Sehemi, A. Irfan, A.M. Asiri, Y.A. Ammar, *J. Mol. Struct.* 1019 (2012) 130–134;
 (b) A.G. Al-Sehemi, A. Irfan, A.M. Asiri, Y.A. Ammar, *Spectrochim. Acta, A: Mol. Biomol. Spectrosc.* 91 (2012) 239–243.
- [20] (a) H.O. Al-Maghamsi, A.A. AlGhamdi, E.-S. Shalaan, High efficiency dye sensitized/metal-nanoparticle composite solar cell, in: Thesis, (2012), Faculty of Science, King Abdulaziz University, Jeddah, Saudi Arabia, 2012;
 (b) G. Frenzer, W.F. Maier, *Ann. Rev. Mater. Res.* 36 (2006) 281–331.
- [21] (a) A.K.K. Kyaw, D.H. Wang, D. Wynands, J. Zhang, T.Q. Nguyen, G.C. Bazan, A.J. Heeger, *Nano Lett.* 13 (2013) 3796–3801;
 (b) L.B. Freund, S. Suresh, *Thin Film Materials: Stress, Defect Formation and Surface Evolution*, Cambridge University Press, New York, 2009.
- [22] (a) A.G. Al-Sehemi, A. Irfan, A.M. Fouda, *Spectrochim. Acta, A: Mol. Biomol. Spectrosc.* 111 (2013) 223–229;
 (b) A.G. Al-Sehemi, R.S.A Al-Amri, A. Irfan, *Acta Phys. Chim. Sin.* 29 (2013) 55–63;
 (c) A. Irfan, M. Nadeem, M. Athar, F. Kanwal, J. Zhang, *Comput. Theor. Chem.* 968 (2011) 8–11;
 (d) A.G. Al-Sehemi, A. Irfan, A.M. Asiri, *Theor. Chem. Acc.* 131 (2012) 1199–1208;
- [23] B.M. Wong, J.G. Cordaro, *J. Chem. Phys.* 129 (2008) 214703–214710.
- [24] R.J. Magyar, S. Tretiak, *J. Chem. Theory Comput.* 3 (2007) 976–987.
- [25] D. Guillaumont, S. Nakamura, *Dyes Pigm.* 46 (2000) 85–92.
- [26] A.G. Al-Sehemi, A. Irfan, A.M. Asiri, *Theor. Chem. Acc.* 131 (2012) 1199–1208.
- [27] (a) A.D. Becke, *J. Chem. Phys.* 98 (1993) 5648–5652;
 (b) C. Lee, W. Yang, R.G. Parr, *Phys. Rev. B: Condens. Matter* 37 (1988) 785–789.
- [28] P.J. Stephens, F.J. Devlin, C.F. Chabalowski, M.J. Frisch, *J. Phys. Chem. A* 98 (1994) 11623–11627.
- [29] B.J. Lynch, P.L. Fast, M. Harris, D.G. Truhlar, *J. Phys. Chem. A* 104 (2000) 4811–4815.
- [30] J.P. Perdew, J.A. Chevary, S.H. Vosko, K.A. Jackson, M.R. Pederson, D.J. Singh, C. Fiolhais, *Phys. Rev. B: Condens. Matter* 46 (1992) 6671–6687.
- [31] Christopher J. Cramer, *Essentials of Computational Chemistry*, John Wiley & Sons, Ltd., Chichester, 2002.
- [32] G.A. Zhurko, <http://www.chemcraftprog.com>
- [33] P.J. Walsh, K.C. Gordon, D.L. Officer, W.M. Campbell, *J. Mol. Struct. THEOCHEM* 759 (2006) 17–24.
- [34] D.M. Cleland, K.C. Gordon, D.L. Officer, P. Wagner, P.J. Walsh, *Spectrochim. Acta, A: Mol. Biomol. Spectrosc.* 74 (2009) 931–935.
- [35] (a) C.R. Zhang, W.Z. Liang, H.S. Chen, Y.H. Chen, Z.Q. Wei, Y.Z. Wu, *J. Mol. Struct. THEOCHEM* 862 (2008) 98–104;
 (b) J. Sun, J. Song, Y. Zhao, W.Z. Liang, *J. Chem. Phys.* 127 (2007) 234107–234113.
- [36] D. Matthews, P. Infelta, M. Grätzel, *Sol. Energy Mater. Sol. Cells* 44 (1996) 119–155.
- [37] (a) A. Irfan, A.G. Al-Sehemi, A. Kalam, *J. Mol. Struct.* 1049 (2013) 198–204;
 (b) A. Irfan, A.G. Al-Sehemi, M.S. Al-Assiri, *J. Mol. Graphics Modell.* 44 (2013) 168–176;
 (c) A. Irfan, A.G. Al-Sehemi, M.S. Al-Assiri, *J. Fluorine Chem.* 157 (2014) 52–57;
 (d) A. Irfan, A.G. Al-Sehemi, M.S. Al-Assiri, *Comput. Theor. Chem.* 1031 (2014) 76–82;
 (e) A.G. Al-Sehemi, A. Irfan, M. Abdullah Asiri, *Chin. Chem. Lett.* 25 (2014) 609–612;
 (f) A. Irfan, A.G. Al-Sehemi, S. Muhammad, *Synth. Met.* 190 (2014) 27–33.
- [38] M. Cossi, V. Barone, *J. Chem. Phys.* 115 (2001) 4708–4717.
- [39] C. Amovilli, V. Barone, R. Cammi, E. Cancès, M. Cossi, B. Mennucci, C.S. Pomelli, J. Tomasi, *Adv. Quantum Chem.* 32 (1998) 227–261.
- [40] J. Tomasi, B. Mennucci, R. Cammi, *Chem. Rev.* 105 (2005) 2999–3094.
- [41] J. Preat, D. Jacquemin, E. Perpete, *Environ. Sci. Technol.* 44 (2010) 5666–5671.
- [42] M.J. Frisch, et al., *Gaussian 09, Revision A.1*, Gaussian, Inc., Wallingford, CT, 2009.
- [43] C.-Y. Liu, Z.C. Holman, U.R. Kortshagen, *Nano Lett.* 9 (2008) 449–452.
- [44] C.Y. Kuo, W.C. Tang, C. Gau, T.F. Guo, D.Z. Jeng, *Appl. Phys. Lett.* 93 (2008) 033303–033307.
- [45] B. Stuart, *Infrared Spectroscopy Fundamentals and Applications*, John Wiley & Sons, Ltd., Chichester, West Sussex, England, 2004, ISBN 0-470-85427-8.
- [46] B.D. Misty, *A Handbook of Spectroscopic Data Chemistry: UV, IR, PMR, CNMR and Mass Spectroscopy*, Oxford Book Co., New Delhi, 2009, ISBN: 9789350430699 935043069X.
- [47] A.M. Asiri, A.A. Bahaj, I.M.I. Ismail, N.A. Fatani, *Dyes Pigm.* 71 (2006) 103–108.
- [48] R. Aich, F. Tran-Van, F. Goubard, L. Beouch, A. Michaleviciute, J.V. Grazulevicius, B. Ratier, C. Chevrot, *Thin Solid Films* 516 (2008) 7260–7265.
- [49] L. Sun, F.Q. Bai, Z.X. Zhao, B.Z. Yang, H.X. Zhang, *J. Polym. Sci., B: Polym. Phys.* 48 (2010) 2099–2107.
- [50] R.K. Chan, S.C. Liao, C. Can, *J. Chem.* 48 (1970) 299–305.
- [51] C.J. Brabec, S. Gowrisanker, J.J.M. Halls, D. Laird, S. Jia, S.P. Williams, *Adv. Mater.* 22 (2010) 3839–3856.
- [52] B.A. Gregg, M.C. Hanna, *J. Appl. Phys.* 93 (2003) 3605–3614.
- [53] V.D. Mihailitchi, H.X. Xie, B. de Boer, L.J.A. Koster, P.W.M. Blom, *Adv. Funct. Mater.* 16 (2006) 699–708.
- [54] C.J. Brabec, A. Cravino, D. Meissner, N.S. Sariciftci, T. Fromherz, M.T. Rispons, L. Sanchez, J.C. Hummelen, *Adv. Funct. Mater.* 11 (2001) 374–380.
- [55] T. Yamanari, T. Taima, J. Sakai, K. Saito, *Sol. Energy Mater. Sol. Cells* 93 (2009) 759–761.
- [56] M.C. Scharber, D. Mühlbacher, M. Koppe, P. Denk, C. Waldauf, A.J. Heeger, C.J. Brabec, *Adv. Mater.* 18 (2006) 789–794.
- [57] X. Yang, J. Loos, S.C. Veenstra, W.J.H. Verhees, M.M. Wienk, J.M. Kroon, M.A.J. Michels, R.A.J. Janssen, *Nano Lett.* 5 (2005) 579–583.